JOM, Vol. 71, No. 1, 2019
https://doi.org/10.1007/s11837-018-3142-3
© 2018 The Minerals, Metals & Materials Society



# Sequential Infiltration Synthesis of $Al_2O_3$ in Polyethersulfone Membranes

RUBEN Z. WALDMAN,[1,2] DEVIKA CHOUDHURY,[3] DAVID J. MANDIA,[3] JEFFREY W. ELAM,[3,5] PAUL F. NEALEY,[1,4] ALEX B.F. MARTINSON,[4] and SETH B. DARLING[1,2,5,6]

1.—Institute for Molecular Engineering, University of Chicago, 5640 S. Ellis Ave, Chicago, IL 60637, USA. 2.—Chemical Sciences and Engineering Division, Argonne National Laboratory, 9700 S. Cass Ave, Lemont, IL 60439, USA. 3.—Applied Materials Division, Argonne National Laboratory, 9700 S. Cass Ave, Lemont, IL 60439, USA. 4.—Materials Science Division, Argonne National Laboratory, 9700 S. Cass Ave, Lemont, IL 60439, USA. 5.—Institute for Molecular Engineering, Argonne National Laboratory, 9700 S. Cass Ave, Lemont, IL 60439, USA. 6.—e-mail: darling@anl.gov

We report the sequential infiltration synthesis (SIS) of aluminum oxide ($Al_2O_3$) into polyethersulfone (PES) ultrafiltration (UF) membranes to form hybrid nanocomposites. SIS relies on chemical interactions between precursor vapors and polymer functional groups, and enables nucleation and growth of inorganic materials to controlled depth. Using in situ Fourier-transform infrared spectroscopy and ellipsometry measurements, we demonstrate that trimethylaluminum associates with the sulfonyl groups in PES, extending the library of SIS-modified polymer nanocomposites to a previously undescribed polymer system and new application space: PES UF membranes. Depth-profiled x-ray photoelectron spectroscopy showed that the trimethylaluminum purge time dictates the extent of $Al_2O_3$ infiltration. Energy dispersive spectroscopy revealed the differences between SIS and atomic layer deposition in the membranes. This work demonstrates the viability of SIS to access the entire macroporous volume of PES UF membranes.

## INTRODUCTION

Sequential infiltration synthesis (SIS) is a materials synthesis technique by which polymers are infused with inorganic materials using alternating exposures to two chemical vapors.[1–3] SIS bears similarities to atomic layer deposition (ALD) in terms of requisite equipment and available chemistries, but it is qualitatively different. In SIS, the first reactant pulse diffuses into the polymer film and interacts with functional groups along the polymer chains, which are distributed throughout the polymer bulk. The initial nucleation in SIS therefore only takes place in systems where association occurs between the vapor precursor species and a moiety within the polymer. For instance, during $Al_2O_3$ SIS in poly(methyl methacrylate) (PMMA), trimethylaluminum (TMA) reacts with the carbonyl (C=O) groups in PMMA via an intermediate complex to form a covalent Al–O–C linkage.[4–6] Subsequent $H_2O$ exposure converts this species to $Al_2O_3$. The associations between polymer functional groups and organometallic vapors and the resulting kinetics of the SIS process have been shown to be sensitive to temperature.[7] Polymer free volume, glassiness, and crystallinity are also understood to play a role in the diffusion–reaction kinetics of SIS.[8,9] SIS will not take place in non-polar polymers such as polystyrene (PS), which lack functional groups that can associate with the precursor species.[10] In subsequent cycles, SIS takes place on the already nucleated inorganic materials (e.g., $Al_2O_3$) in addition to any unreacted amenable functional groups that remain on the polymer backbone. The inorganic material loading within the polymer can be tuned by parameters including precursor dosage, purge time, temperature, and number of SIS cycles.

Polymers infiltrated with inorganic materials via SIS have found a number of applications in recent reports.[11–24] Two major categories of SIS implementation have been realized. In the first category, the polymer serves as a spatial template for nanoscale


(Published online September 24, 2018)

oxide feature synthesis, and the polymer template is subsequently removed by plasma etching or burn-out. In the second category, the polymer is retained and the resultant polymer-oxide nanocomposite is utilized.

In the first category, polymer resists such as SU-8 can be patterned via conventional lithographic techniques to define features for oxide infiltration.[11,12] Ultrathin arrays of ZnO nanowires fabricated in this way have been used as photodetectors.[13] Lithographic limits can be overcome by using block copolymers (BCPs), which self-assemble into nanoscale patterns (spheres, lamellae, cylinders, etc.) with dimensions dictated by molecular weight and penalty of mixing between blocks.[25] The chemical incompatibility between the two blocks enables selective SIS in BCPs. In BCPs, one block, such as PS, does not associate with the precursor species, whereas the other block, such as PMMA or poly(vinyl pyridine) (PVP),[14] does associate. After reaction of the associated precursor, and after all organics are subsequently removed, nanostructured oxides replicating the SIS-active block morphologies remain. BCP-derived oxide nanostructures fabricated via SIS have found utility as lithographic hard masks,[15] anti-reflective coatings,[16] and isoporous membranes for protein separations.[17]

In the second category, SIS has been used to form polymer-oxide nanocomposites for enhanced lithographic applications. Aluminum oxide and zinc oxide have been used to enhance the etch resistance of electron beam lithography resists for high-aspect-ratio pattern transfer.[18,19] Such nanocomposites have interesting mechanical properties—incorporation of ZnO by SIS into lithographically defined polymer pillars yielded nanocomposites with ultra-high modulus of resilience.[20] SIS of $Al_2O_3$ into polyethylene terephthalate fibers has also been demonstrated to improve mechanical properties and introduce photoluminescent functionality.[9,21] SIS has been used to introduce hydroxyl groups to serve as linkages for silanization chemistry in porous polymeric materials. This functionalization scheme was recently used to convert conventional polyurethane sponges into selective and reusable oil adsorbents.[22,23] SIS has also found use in the otherwise challenging three-dimensional characterization of BCPs. To achieve this, SIS is used as a contrast stain for the PMMA blocks in PS-*b*-PMMA to generate tomographic transmission electron microscopy maps.[24]

In this work, we extend the library of SIS-modified polymer nanocomposites to a previously undescribed polymer system and new application space—polyethersulfone (PES) ultrafiltration membranes. The chemical formula of PES and the microporous structure of a typical ultrafiltration membrane formed via phase inversion are displayed in Fig. 1. PES is a hydrophilic polymer extensively used in ultrafiltration; it is desirable for its high-

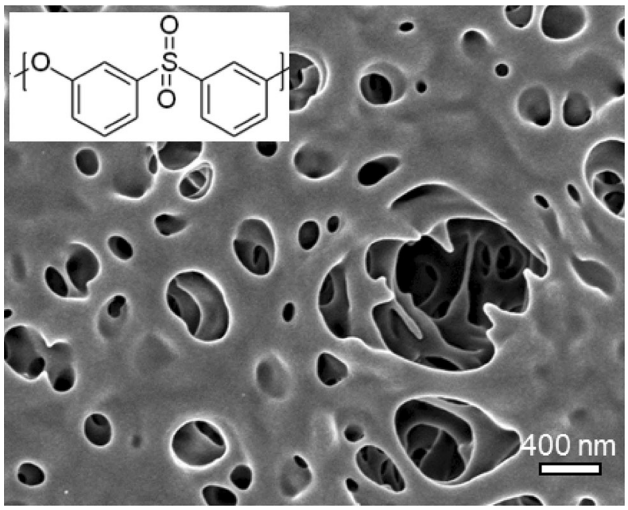


Fig. 1. The chemical structure of polyethersulfone is shown over an SEM image of the surface of a typical polyethersulfone membrane formed via phase inversion with a 200-nm average pore size. Note that the pore geometry is highly polydisperse and tortuous.

temperature stability and mechanical strength imbued by its aromatic–sulfone linkage.[26] There exists a wide literature of modifications to PES membranes to improve performance and lifetime.[27,28] Inorganic materials such as $Al_2O_3$ have been introduced into PES membranes by a number of techniques. The simplest of these is adding oxide nanoparticles to the polymer solution that is then cast to form a membrane.[29–31] Inorganic oxides can also be added to pre-cast extant membranes, for example, by hydrothermal sol–gel methods.[32] In these processes, the resulting coverage over the pore surface is inconsistent, and pores can be blocked by the post-deposition of materials.

Vapor phase processes, such as ALD, provide the possibility for a conformal coating of inorganic oxides on the complex and tortuous pore surfaces of polymeric membranes, thus limiting pore blockage.[33–36] ALD was first demonstrated on flat PES films via a plasma-enhanced $Al_2O_3$ process.[37] ALD $TiO_2$ coating of porous PES membranes has been demonstrated using various precursors.[38,39] In the context of these reports, we have explored the interactions between TMA and the PES functional groups in the first PES SIS process. Whereas ALD-treated membranes have conformal metal oxide coatings that begin in the near-surface of the polymer, SIS-treated membranes are a hybrid nanocomposite directly templated by the initial PES template. SIS has been performed on a polycarbonate membrane that was then calcined to demonstrate the penetration depth of the process.[6] In this paper, SIS is intentionally applied to membranes to explore how hybrid nanomaterial phase-inversion membranes can be achieved.

We use in situ Fourier-transform infrared (FTIR) absorption spectroscopy to elucidate the mechanism by which TMA interacts with PES. In situ FTIR enables detailed study of the interaction chemistry by measuring the distinct vibrational frequencies absorbed by the SIS precursor vapors, the polymer functional groups, and the solid-phase products of their interactions.[10] These measurements provide evidence for the complexation of TMA with the S=O sulfonyl groups in the PES. The conclusions drawn from FTIR are supported by density functional theory (DFT) calculations. We also use in situ spectroscopic ellipsometry to track changes in the optical properties of the PES film *during the SIS process*, from which we infer changes in thickness and refractive index. The effects of SIS processing on the resulting nanocomposite film are further studied by depth-profiled x-ray photoelectron spectroscopy (XPS) to show how the $Al_2O_3$ loading in the polymer can be controlled by the choice of purge time.

Following these mechanistic studies, we performed $Al_2O_3$ SIS to PES membranes formed via phase inversion. Pure water flux measurements reveal a modest reduction in flux in both SIS- and ALD-modified membranes, which can be attributed to pore constriction. In ALD, pore constriction occurs by the deposition of material on the pore surface, while in SIS the pore itself shrinks as the polymer is swelled by the infiltrated oxide. These findings demonstrate that SIS modifies the polymer bulk, whereas ALD only affects the near-surface of the polymer material. Plane-view and cross-sectional energy dispersive spectroscopy (EDS) measurements were performed on the SIS- and ALD-modified PES membranes. Notably, membranes treated with three SIS cycles and 50 ALD cycles have a similar $Al_2O_3$ loading. Moreover, cross-sectional EDS measurements of the SIS-treated membrane showed uniform Al concentrations throughout the entire PES membrane thickness, while similar measurements of the ALD-treated samples showed high Al concentrations near the surface but virtually no Al in the middle. These differences stem from the different timescales of vapor exposures between the two methods,[40,41] and highlight the sensitivity of polymeric substrates to vapor modification conditions.

## MATERIALS AND METHODS

### Infrared Spectroscopy

PES polymer pellets ($M_w$ = 58 kg/mol) were purchased from Goodfellow Cambridge, dissolved in dimethyl formamide (DMF) at a 4 wt.% solution and spin-coated at 3000 rpm to achieve a ~ 150-nm film. The polymer was spun onto double-sided polished undoped silicon wafers to minimize IR absorption by the substrate. The samples were prepared in an argon-filled glovebox, as spin-coating in air was found to yield rough and inconsistent films due to non-solvent-induced phase separation via ambient humidity (supplementary Fig. S-1).[42]

In situ FTIR measurements were performed using a Nicolet 6700 FTIR spectrometer (Thermo Scientific) interfaced to a custom ALD reactor, as described previously.[43] Each FTIR spectrum represents an average of 64 scans taken at 4 $cm^{-1}$ resolution over the 400–4000 $cm^{-1}$ spectral range, and the signal intensity was calculated as an absorbance. FTIR measurements were conducted at a constant temperature of 110°C. The PES-coated substrates were allowed to equilibrate in flowing, ultrahigh-purity (99.999%) $N_2$ using a 300-sccm flow rate at 3.5 Torr pressure within the heated reactor for 2 h before the beginning of the experiment. A long bake in the chamber was used to drive off solvent, as residual Lewis-basic solvents such as DMF have been shown to play a potential role in SIS nucleation.[44]

### Density Functional Theory (DFT) Calculations

DFT calculations were performed using Gaussian 09 software.[45] Isolated polymer fragments and TMA precursor were first geometrically optimized at the B3LYP/6-31G(d,p) level to ascertain their equilibrium free energies. The two species were then optimized in proximity to search for potential weak-binding interactions associated with SIS processes, as has been reported with TMA and PMMA.[4] Energy differential between any such bound species and the isolated fragments provides an approximation for the potential energy well of the complex.

### Spectroscopic Ellipsometry

PES films with a thickness of 60 nm were spin-coated onto silicon wafer pieces from a solution of 2.5 wt.% polymer in DMF in a glovebox. In situ spectroscopic ellipsometry was performed using a J. A. Woollam M-2000 V with spectral range of 380–1000 nm at a fixed angle of 70° interfaced to an Ultratech Fiji ALD Chamber. Ellipsometric spectra were collected through Ar-purged windows every 2.5 s. PES samples were introduced into the chamber and held at the process temperature of 110°C for 45 min prior to beginning the SIS process to remove any residual water or other solvents. A 15-s TMA pulse followed by 5 min of exposure (valve to exhaust pump closed) was performed to saturate the film with TMA. After this exposure, the pump valve was opened to purge the chamber for a controlled duration. Following this purge step, an identical water pulse, exposure, and purge were conducted, completing the SIS cycle.

Spectroscopic ellipsometry tracks the change in polarization of light as it reflects off a thin film sample and is measured as an amplitude ratio $\psi$ and a phase angle $\delta$ over a range of wavelengths (380–1000 nm in this study). These data are fit to the Cauchy model, which describes the wavelength-

dependent refractive index by the following equation:

$$n(\lambda) = A + \frac{B}{\lambda} + \frac{C}{\lambda^2} \quad (1)$$

where $n$ is the refractive index at a particular wavelength. $A$, $B$, and $C$, along with the thickness of the film, are fitting parameters and are varied using software to optimize agreement between the model and the collected data. Throughout the SIS process, the Cauchy model was used to fit the collected spectroscopic ellipsometry data.

### X-ray Photoelectron Spectroscopy

XPS surface analysis measurements were carried out on a Thermo Scientific K-Alpha+ using a microfocused monochromatic Al K$\alpha$ (1487 eV) x-ray source with a spot size of 400 $\mu$m. Samples were affixed to the transfer stage mount using Cu clips, and depth profiling measurements were performed with an $Ar^+$ bombardment voltage of 3 keV (low-current) with 5 s per sputter cycle and corresponding effective etch rate of $\sim$ 0.25 nm/s. Raster area of the depth profiles was $2 \times 2$ mm$^2$ (effectively $5 \times$ the x-ray spot size) wide-scan surveys, and high-resolution XPS snapshots for the Al 2p, O 1s, C 1s, Si 2p, and S 2p regions were collected after each sputter cycle, and 100 sputter cycles (500 s total sputtering time) were performed on each sample. Batch fitting and processing of the HR-XPS snapshots were performed in Thermo Advantage 5.977 software, and mixed Gaussian–Lorentzian peak shapes were used in all fitting routines in the aforementioned regions of interest. Due to overlap of the S 2p region with the Si 2s plasmon loss peak at the interface ($\sim$ 162–165 eV) and closer to the substrate, the S 2p signal was normalized to the depletion rate of the O 1s signal at the interfacial regions of each sample ($\sim$ 130–150 s). Because of this overlap, the S 2p region could not be constrained to a particular binding energy value in the batch-fitting process without also including the Si 2s signal.

### Membrane Fabrication

Both SIS and ALD of the PES membranes were performed on an Ultratech Savannah ALD Chamber held at 110°C. Membranes were held at the process temperature for at least 20 min to drive off moisture. ALD processes were conducted in flow mode with a single cycle consisting of a .015-s TMA pulse, a 10-s purge, a .015-s $H_2O$ pulse, and a 10-s purge. The number of cycles performed ranged from 50 to 600. SIS processes were conducted in exposure mode, using a stop valve to keep the reactants in the chamber. A 1-s dose of TMA was held in the chamber with a closed stop valve for 5 min, followed by opening the stop valve for a 30-s purge and a 4-s water pulse with a 5-min exposure with closed stop valve. Membranes were prepared with 1, 3, 5, and 7 SIS cycles. The membranes were suspended above the base of the ALD chamber by securing them between glass slides at both edges. This allowed for unhindered vapor flow on both faces of the membranes.

### Dead-End Filtration

Flux measurements were taken using an Amicon Stirred Cell Model 8010 using nitrogen gas at a pressure of 10 psi using reverse osmosis-treated water. Permeate was collected in a beaker on a balance, and a Labview program collected the mass of permeate over time. Three samples at each condition were measured a total of three times, and the average flux normalized by pressure was calculated according to the following equation:

$$\frac{F}{P} = \frac{\Delta V}{\Delta t * A * P} \quad (2)$$

$F$ is flux, $V$ is volume of permeate, $t$ is time, $P$ is the transmembrane pressure, and $A$ is membrane area. An effective membrane diameter of 25 mm was used in this calculation, and the results were converted to L/h/m$^2$/bar.

### Membrane Characterization

Polyethersulfone membranes (200 nm nominal pore size, 150 $\mu$m thickness, 25 mm diameter) were purchased from Sterlitech. Differential scanning calorimetry (DSC) was conducted on both membrane and polymer pellets on a TA Instruments Discovery DSC 2500 from $-$ 50°C to 275°C at a rate of 10°C/min. Size-exclusion chromatography (SEC) measurements were conducted on a Shimadzu Prominence High Performance Liquid Chromatograph system using an eluent mobile phase of DMF with 0.01 M LiBr at a flow rate of 0.4 mL/min. Separation was achieved using a TSKgel SuperAW4000 column (TOSOHBioscience) maintained at ambient temperature with pore sizes suitable for materials with effective molecular weights from $\sim$ 1000 g/mol to 500,000 g/mol. The differential refractive index signal was collected using a Wyatt Optilab T-rEX differential refractometer ($\lambda$ = 658 nm). Molar mass distributions were determined relative to narrow-dispersity polystyrene standards using Wyatt Astra VII software.

Membrane samples for elemental analysis were prepared in cross-section by submersion into liquid nitrogen for 1 min and then cracking along a notch prepared by a razor blade. The cleaved edge of the broken membrane was adhered to the vertical edge of a SEM sample stub using copper tape such that the top face of the membrane in the ALD chamber side faced away from the sample stub. The membrane's broken edge was aligned to be flush with the lip of the stub wall. The sample was coated with 4 nm of carbon to mitigate charging. EDS

measurements were conducted on a TESCAN LYRA3 field-emission scanning electron microscope with an accelerating voltage of 10 keV and a working distance of 9 mm. EDS map spectra were collected using two Oxford Instruments X-MaxN detectors and analyzed using the AZtec software package. The EDS x-ray signal centered at 1.486 keV corresponding to the aluminum $K\alpha_1$ peak was mapped across the membrane cross-section to generate a bit-map image of the signal intensity. Mapping scans were taken at an image magnification of ×5000 and at a 512-pixel resolution. The energy range and channel number were set to auto, and a process time of 4 $\mu$s and a pixel dwell of 50 $\mu$s were used. The mapping scan data were binned along the axis parallel to the membrane to generate 2D plots of Al concentration versus depth.

## RESULTS AND DISCUSSION

### In Situ FTIR Spectroscopy

The absorption of TMA in a PES film was first studied by recording FTIR spectra after sequential 10-s pulses of TMA. To avoid growing $Al_2O_3$ on the IR-transparent KBr windows, gate valves between the SIS and chamber were closed during the 10-s SIS precursor exposures and the 30-s purges. Including the time needed to record the spectra, ~ 110 s of TMA purge and out-diffusion occurred between each TMA dose. The PES absorption spectrum shown in black at the bottom of Fig. 2a has been reduced in scale relative to the other spectra for clarity. The main peaks in the PES absorption spectrum are listed in Table I, and the assignments are based on previous infrared studies

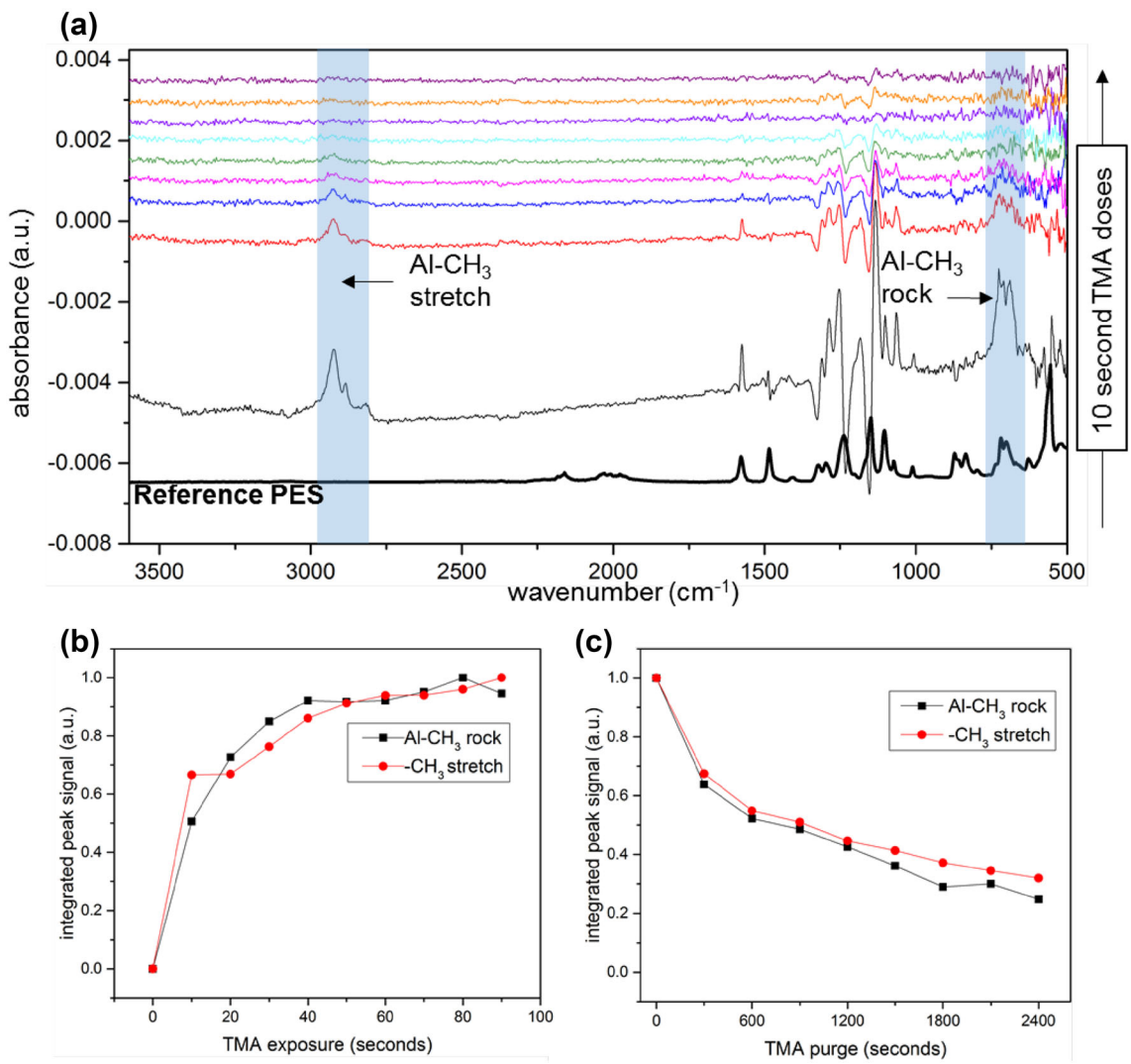


Fig. 2. (a) Difference spectra of PES films after successive 10-s doses of TMA show the gradual saturation of the TMA signal as measured by the Al-$CH_3$ stretch and rock vibrations. (b) Integration of these two modes reveals the kinetics of the saturation of TMA within the film. (c) Integration of the Al-$CH_3$ modes upon purging at 5-min intervals reveals slow kinetics of out-diffusion.

of PES and related compounds.[46–48] Figure 2a displays the difference spectra between sequential doses that have been offset vertically for clarity. The spectra are referenced to the initial PES absorption spectrum in bold at the bottom of the figure. Consequently, positive-going peaks indicate newly created species, while negative-going peaks indicate species consumed during the TMA exposure. The blue-shaded regions highlight the C–H stretching region for Al-$CH_3$ at 2923 $cm^{-1}$ and the C–H rocking features for Al-$CH_3$ at 700 $cm^{-1}$.[4,49,50] These features are consistent with TMA absorbed within the PES film. Relatively large increases in the C–H stretching and rocking regions appear during the first TMA exposure, but these changes diminish with additional TMA exposure and saturate after ~ 60 s. Figure 2b shows the normalized integrated intensities of these spectral regions versus TMA exposure time, and demonstrates that the C–H stretching and rocking features follow the same absorption kinetics, as expected for features deriving from the same chemical species. Supplementary Fig. S-2 shows the baseline-corrected peaks from which these integrated plots were taken, which are all referenced to the initial PES spectrum. The other features in the spectra will be discussed later in the context of the TMA + PES interaction mechanism.

Following this cumulative 90-s TMA exposure, spectra were collected every 5 min during a continuous TMA purge period to observe any changes in the concentration or bonding of the absorbed TMA. Difference spectra for this sequence are plotted in supplementary Fig. S-3 and show the gradual reduction in intensity for the C–H stretching and rocking features. Integration and normalization of these peaks (Fig. 2c) reveals that TMA is slowly released from the PES on a timescale ~ 100 × slower compared to the uptake of TMA. After 40 min of purging, ~ 70% of the integrated absorption intensity is lost, corresponding to ~ 30% of the initial saturated TMA retained in the film. The film was then quenched with a water pulse to complete one SIS cycle, the spectral features of which are discussed later.

**Table I. PES vibrational features and assignments[46–48]**

| Peak position ($cm^{-1}$) | Assignment |
|---|---|
| 1483 | Aromatic C=C stretch |
| 1322 | Asym O=S=O stretch |
| 1297 | Asym O=S=O stretch |
| 1241 | C–O–C stretch |
| 1149 | Sym O=S=O |
| 1105 | Aromatic ring vibration |
| 1071 | Aromatic ring vibration |
| 1011 | Aromatic ring vibration |

Following this initial $Al_2O_3$ SIS cycle in the PES film, four additional TMA/$H_2O$ SIS cycles were performed. Each SIS cycle consisted of a 60-s TMA exposure, 60-s purge, 60-s $H_2O$ pulse, and another 60-s purge. FTIR spectra were recorded after each TMA and $H_2O$ purge. Figure 3a shows difference spectra in the high-frequency region after each exposure referenced to the initial PES film. The C–H stretching peaks at 2923 $cm^{-1}$ appear with each TMA exposure and are extinguished with each water exposure. Presumably, $H_2O$ reacts with the infiltrated TMA species and generates methane, which diffuses out of the polymer. This spectral change diminishes with additional SIS cycles so that after four SIS cycles the spectrum no longer appreciably changes. This most likely results from a constriction of the PES free volume diffusive pathways required for TMA and $H_2O$ to reach reactive sites. Figure 3b shows difference spectra in the low-frequency region of successive $H_2O$ exposures referenced to the initial PES film. The feature centered at 800 $cm^{-1}$ is the broad Al-O phonon mode of $Al_2O_3$.[51] This peak continues to increase over the first three SIS cycles, but flattens as less $Al_2O_3$ is grown with each cycle. This supports the hypothesis that SIS continues for approximately three SIS cycles but then terminates.

The preceding discussion focused primarily on the TMA Al-$CH_3$ peaks in order to understand the kinetics for TMA absorption and desorption and the effects of multiple cycles. However, a close examination of the changes in the PES vibrational features upon TMA absorption can yield additional insights into the mechanism of the TMA-PES interaction. Figure 2a shows significant changes in the 1000 and 1500 $cm^{-1}$ regions upon TMA exposure. These changes are highlighted in Fig. 4. The reference PES spectrum at the bottom of Fig. 4 shows peaks at 1483 (aromatic C=C stretch), 1322

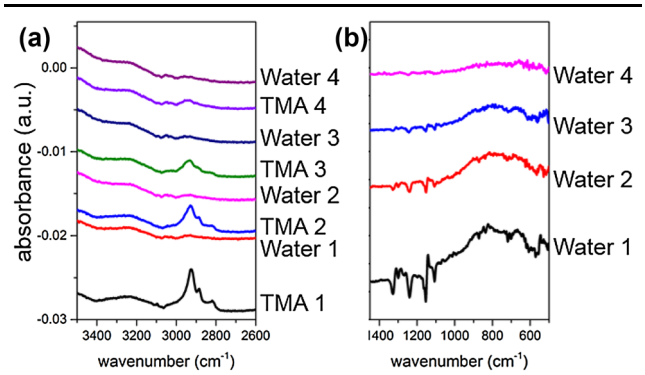


Fig. 3. (a) Difference spectra between successive TMA and water exposures with reference to PES reveal the appearance of TMA methyl features and their extinction upon water dosing. The intensity of the infiltrated methyl signature decreases as sites along the polymer are consumed and as already formed oxide acts as a diffusion barrier. (b) Difference spectra between the water exposures of four SIS cycles reveal the emergence of an Al-O phonon mode. The signal gain decreases over successive cycles.

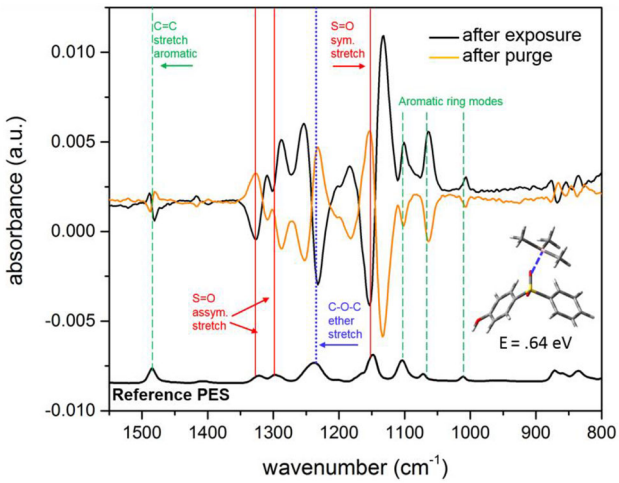


Fig. 4. Difference spectra between PES and 90 s of cumulative TMA exposure (black) and 40 min of TMA purging (orange) reveal the reversibility of the spectral shifts caused by association between TMA and PES. C–C modes (green), S=O modes (red), and C–O modes (blue) that undergo changes due to TMA complexation are indicated. The inset shows a DFT calculation for the equilibrated structure between TMA and the sulfonyl group of the PES monomer (Color figure online).

and 1297 (asymmetric S=O stretch), 1241 (asymmetric C–O–C stretch), 1149 (symmetric S=O stretch), and at 1105 $cm^{-1}$, 1071 $cm^{-1}$, and 1011 $cm^{-1}$ (aromatic ring modes). These peaks have been color-coded in Fig. 4 to highlight the C–C (green), S=O (red), and C–O (blue) modes.

Following 90 s of TMA exposure (black spectrum), both positive- and negative-going features emerge corresponding to the creation and consumption of species, respectively. The largest of these changes corresponds to an intensity loss of $\sim$ 4%, indicating that TMA occupies 4% of the available sites. In the case of the lower frequency aromatic ring modes, only positive peaks are seen. For the S=O modes (red), we see negative peaks indicating consumption of S=O species, accompanied by a positive peak at $\sim$ 25 $cm^{-1}$ lower frequency (i.e., red-shifted). Conversely, for the C–O peak at 1241 $cm^{-1}$ (blue) and the 1483 $cm^{-1}$ aromatic stretch, there is a negative feature accompanied by a positive peak at 10–30 $cm^{-1}$ higher frequency (blue-shifted). We note that all of these changes are reversible upon prolonged purge as evidenced by the yellow spectrum in Fig. 4 recorded following 40 min of TMA purge. This spectrum is referenced to the spectrum recorded after TMA exposure (black spectrum), and is essentially a mirror image. Based on previous in situ FTIR studies of the interaction between TMA and PMMA,[4,5] we attribute the spectral changes to the S=O peaks to the formation of a weakly bound intermediate complex that weakens the S=O bond thereby shifting it to lower frequency:

$$Al(CH_3)_3 + S = O \leftrightarrow S = O - - - Al(CH_3)_3 \qquad (3)$$

Similarly, the blue-shifted C–O peaks result from TMA physisorbed to the oxygen atoms on the ester groups, and the blue shift is a consequence of a resonance effect.[52] As indicated in Eq. 2, the physisorbtion is reversible, and this results in TMA desorption to reform the S=O species so that the spectral changes reverse. It is not as clear why the low-frequency ring modes increase upon TMA exposure, but these changes are also reversed during the purge step.

A DFT simulation of an isolated PES monomer and TMA molecule was performed to see if this proposed weakly bound intermediate proposed in Eq. 1 is energetically plausible. These simulations show that there is indeed an attractive association related to the sulfone groups of the polymer. The inset in Fig. 4 shows an equilibrated configuration with a binding free energy of 0.64 eV. This simulation supports our hypothesis that the SIS reaction between TMA and PES is qualitatively similar to that between TMA and PMMA, albeit with a different binding strength.[4,5]

Supplementary Fig. S-4 shows an FTIR spectrum of the PES before SIS (red) and following the $H_2O$ exposure of the first SIS cycle (blue, scaled by 100 $\times$) referenced to the PES spectrum. We note that there is a net decrease in the intensity of all the peaks described above in the context of the weakly bound intermediate. The magnitude of these changes is $\sim$ 1% of the initial spectral intensity, indicating that $\sim$ 1% of the S=O bonds are permanently broken because of the SIS. We attribute this behavior to the formation of $Al_2O_3$ in the bulk of the PES, where some of the methyl groups from the TMA remain bound to the S or to the aromatic ring. Residual methyl groups bound to carbon atoms in the aromatic rings would account for the net loss in intensity of the aromatic ring vibrational features following the SIS.

One other feature of note in Fig. 4 is the loss of signal at 1231 $cm^{-1}$, representing the C–O–C aryl ether stretch. In a study of TMA and polyethylene oxide (PEO), which is composed of C–O–C bonds, a loss of absorption at 1100 $cm^{-1}$ was ascribed to TMA cutting ether bonds at that position.[6] Although much of the intensity drop at 1231 $cm^{-1}$ during the TMA exposure is recovered during the subsequent purge, we do observe a net decrease following the $H_2O$ exposure (supplementary Fig. S-4). This indicates that both the S=O and the C–O serve as nucleation sites for the $Al_2O_3$ SIS in PES.

These FTIR measurements confirm that TMA associates with the sulfonyl and aryl ether groups of the PES polymer in a qualitatively similar way to the association with the carbonyl and ester groups of PMMA. These data enable mechanistic comparisons between SIS in PES and PMMA—comparisons of the binding strength and extent of reaction are complicated by the different glass transition temperature, polymer free volume, and TMA solubility and diffusivity in different polymers.[8] The

saturation/purge study presented shows an equal rate of association/dissociation between the proposed interactions, as the peak shifts recover identically. Further temperature studies of this process could reveal whether these different sites of association along the PES backbone have different energetics. Studying longer purge times could also provide evidence for the direct conversion of PES-TMA complexes into covalent bonds.

### In Situ Spectroscopic Ellipsometry and Depth-Profiled XPS Measurements

A challenge inherent to kinetically controlled SIS process design is that any of a number of environmental factors can influence the extent of precursor infiltration and partially reversible removal, which alter the hybrid material product. In order to gain insight into this complexity, one must observe the film during the SIS process itself.

As shown in Fig. 5, in situ ellipsometry was used to track the thickness and refractive index over a 5-min TMA exposure, followed by a 25-min purge. This sequence reveals an initial film thickness of ~ 60.5 nm with an index of refraction at 538 nm of 1.67. As TMA is introduced into the chamber, the film undergoes rapid swelling over the first ~ 40 s followed by much slower swelling. This is similar to the saturation time observed via FTIR measurements, though differences in the chamber set-up and exposure sequence limit the value of direct comparisons. The refractive index was observed to decrease in tandem with the film thickness increase. This suggests that TMA absorbed by the film swells the material and reduces the film density. At the end of the 5-min exposure, the film thickness increased by 50.0% to 90.8 nm, and the index of refraction decreased by 4.2% to 1.59. As the TMA is purged, the thickness and refractive index partially recover as TMA diffuses out of the polymer film. After 25 min of purging the film, thickness decreased from the saturated thickness of 90.8 nm by 29.7% to 63.8 nm. At an equivalent point of purging in the FTIR measurements, the film had lost ~ 40% of the absorbed TMA as measured by C–H peak intensity. Study of extended purge times using this technique and in situ FTIR may reveal irreversible association of TMA with PES. The precise relationship between the degree of TMA association and the swelling of the film is unclear and also merits further study.

Following the 25-min purge, the PES film was exposed to another 5 min of TMA vapor to saturate it once again. In this second exposure, the film reached a maximum of thickness of 91.1 nm with a corresponding refractive index of 1.60. The slightly higher refractive index of the film upon a second saturation suggests a denser film, but the thickness is incrementally higher. This shows how sensitive polymer films are to precursors such as TMA and how important sample history is in the SIS process. Changes in chain conformation and polymer free volume that may occur during the first TMA infiltration can be retained even after TMA leaves, as the polymer is well below its glass transition temperature. These effects may change how TMA can infiltrate into the polymer in subsequent exposures. As Fig. 5 shows, the sample was then purged for 3 min. The thickness decreases, and the refractive index increases, as the film densifies. The film is quenched with a 15-s water pulse held in exposure mode for 5 min. An abrupt change in the ellipsometry data is observed—the refractive index drops to 1.56, and the thickness drops to 67.2 nm. The loss of

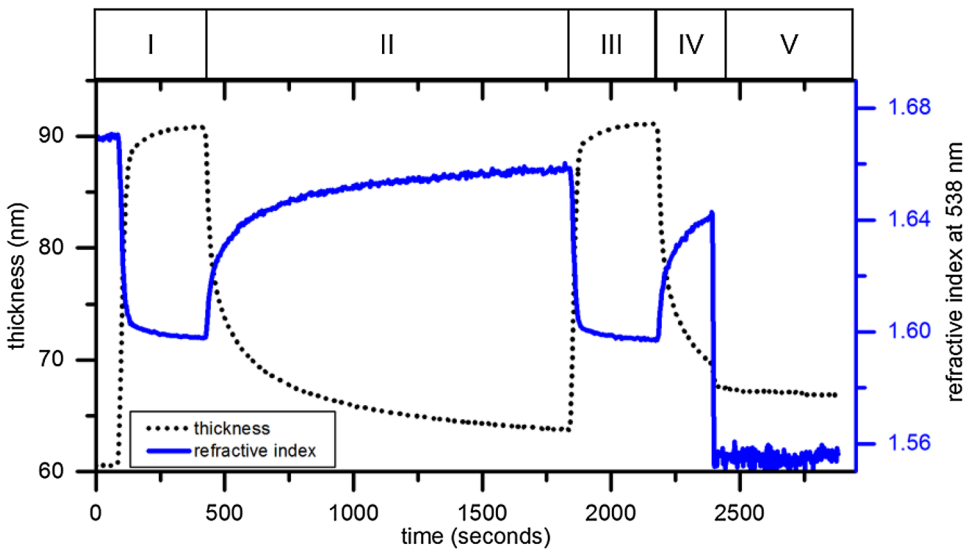


Fig. 5. In situ spectroscopic ellipsometry data fit to a Cauchy model yields a dynamic view of film thickness and refractive index throughout TMA exposure, purging, and $H_2O$ exposure in a SIS process. The plotted sequence tracks a first 5-min TMA exposure (I) followed by a 25-min purge (II), followed by a second 5-min TMA pulse (III), a 3-min purge (IV), and a 5-min quenching water exposure (V).

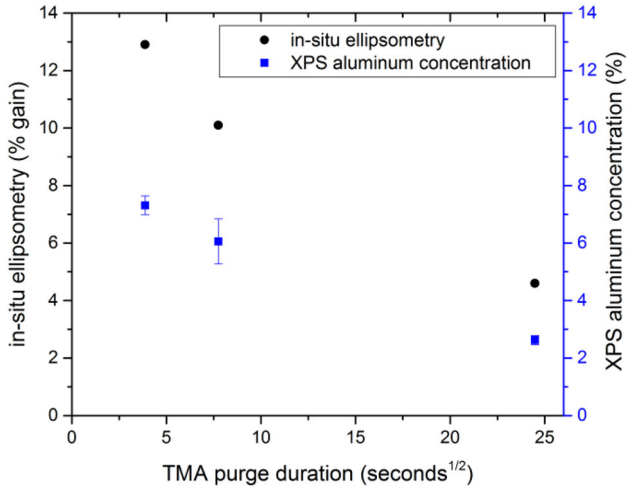


Fig. 6. Percentage increase in PES film thickness as measured by in situ spectroscopic ellipsometry (black) and averaged aluminum concentration as measured by depth-profiled XPS (blue) versus TMA purge time following 6-min TMA exposure (Color figure online).

thickness with water exposure is not instantaneous, and a decay over several seconds is observed. This may be attributed to the liberation of gas-phase products such as methane that diffuse out of the film. The rapid change in refractive index occurs with the formation of solid-phase $Al_2O_3$. Future studies employing more sophisticated models than a single Cauchy layer may reveal further insights into how the polymer-inorganic nanocomposites evolve throughout the SIS process.

Figure 6 shows the different percentage gains in thickness for equivalent 60-nm-thick PES films that were exposed to TMA for 5 min and then quenched with water after 15-s, 1-min, and 10-min purges. The marked non-linearity of the increased purge time confirms that the loss of TMA is a diffusion process, as deduced for previous SIS systems. Figure 6 also shows the resulting average aluminum content in the three films as measured by depth-profiled XPS measurements. These data were constructed by averaging the aluminum content measured after each incremental etch. Elemental distributions of these films are included in supplementary Fig. S-5. An unprocessed PES film was found to have a uniform distribution of 0.7% Al composition, which was attributed to aluminum contamination of the XPS tool. The uniformity of the aluminum and oxygen features observed across 60 nm demonstrates that the TMA dose and exposure gave sufficient time for the TMA vapor to diffuse fully into the film to result in a nearly uniform distribution. The 60-nm thickness is significantly shorter than the diffusion depth of TMA through PES under the selected processes conditions. In the limit of a bulk polymer film, one would expect the infiltrated oxide to have a decreasing concentration profile deeper in the film as a consequence of diffusion limitation. Supplementary Fig. S-6 compares the oxygen 1s peaks from 530 eV to 535 eV and the aluminum 2p peak at 74.7 eV, showing the control PES film and the 1-min purge SIS sample. The introduction of a peak at 531.45 eV represents the inclusion of contributions from the Al-O bonding environment. Likewise, the Al 2p peak is completely absent in the unmodified PES film.

## SIS in Porous PES Ultrafiltration Membranes

In order to demonstrate the implementation of SIS into membranes, a commercially available UF product was used. Supplementary Figs. S-7 and S-8 show results from DSC and SEC that the PES stock material and the membranes have comparable glass transition temperatures and molecular weight distributions, enabling comparison of the two materials. Figure 7 shows pure water flux data of membranes prepared by a typical SIS recipe and a typical ALD recipe normalized to the flux through an unmodified control membrane. The absolute flux data are plotted in Supplementary Fig. S-9. Even over the short timescales of the ALD recipe, TMA will infiltrate into the PES. In amenable polymers, ALD recipes may be thought of as extremely brief SIS recipes. At ALD timescales, the infiltrated depth is limited to the immediate subsurface of the polymer. All the treated membranes show a decrease in flux relative to the as-received PES membranes, which were measured to have a pressure-normalized flux of 1458 L/h/m$^2$/bar. Notably, a similar reduction in flux was observed between 50 ALD cycles and 3 SIS cycles. More ALD cycles caused a more precipitous decline in flux than increased SIS cycles as described below.

Moderate ALD loading of membranes with metal oxides has been reported to increase their pure water flux.[53] In that report, a hydrophobic polypropylene membrane was treated, and the hydrophilic oxide surface lent a significant flux increase. Such conformal treatments lead to a balance between pore size reduction and enhanced fluid flow. For example, in the treatment of ceramic membranes with ALD N-doped $TiO_2$, which is extremely hydrophilic under light exposure, an initial flux increase is observed at low cycle numbers because the surface enhancement outweighs pore constriction.[54] However, with more cycles, pore constriction will ultimately outweigh the enhanced surface.[36] The PES membranes in this study are initially hydrophilic—PES is generally considered a high-flux membrane material. Therefore, $Al_2O_3$ is not intended nor expected to impart a significant hydrophilicity improvement to the membrane.

The flux decline in the modified membranes is attributed to the constriction of the pore volume due to the introduction of $Al_2O_3$. The fact that many ALD cycles are required to achieve similar flux declines to only a few cycles of SIS highlights the subsurface-limited reactions that take place with ALD recipes

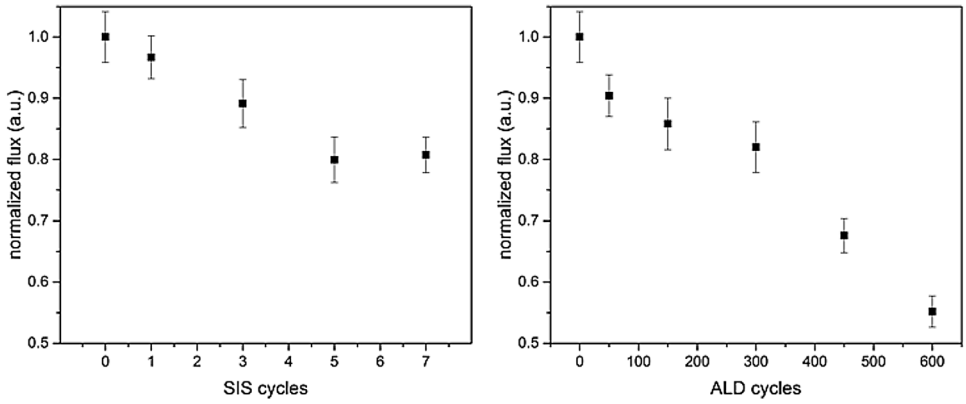


Fig. 7. Pure water flux measurements of both ALD- (right plot) and SIS-modified (left plot) membranes reveal the continuous decline of flux with increasing ALD cycles and the stabilization of flux decline once five SIS cycles are reached.

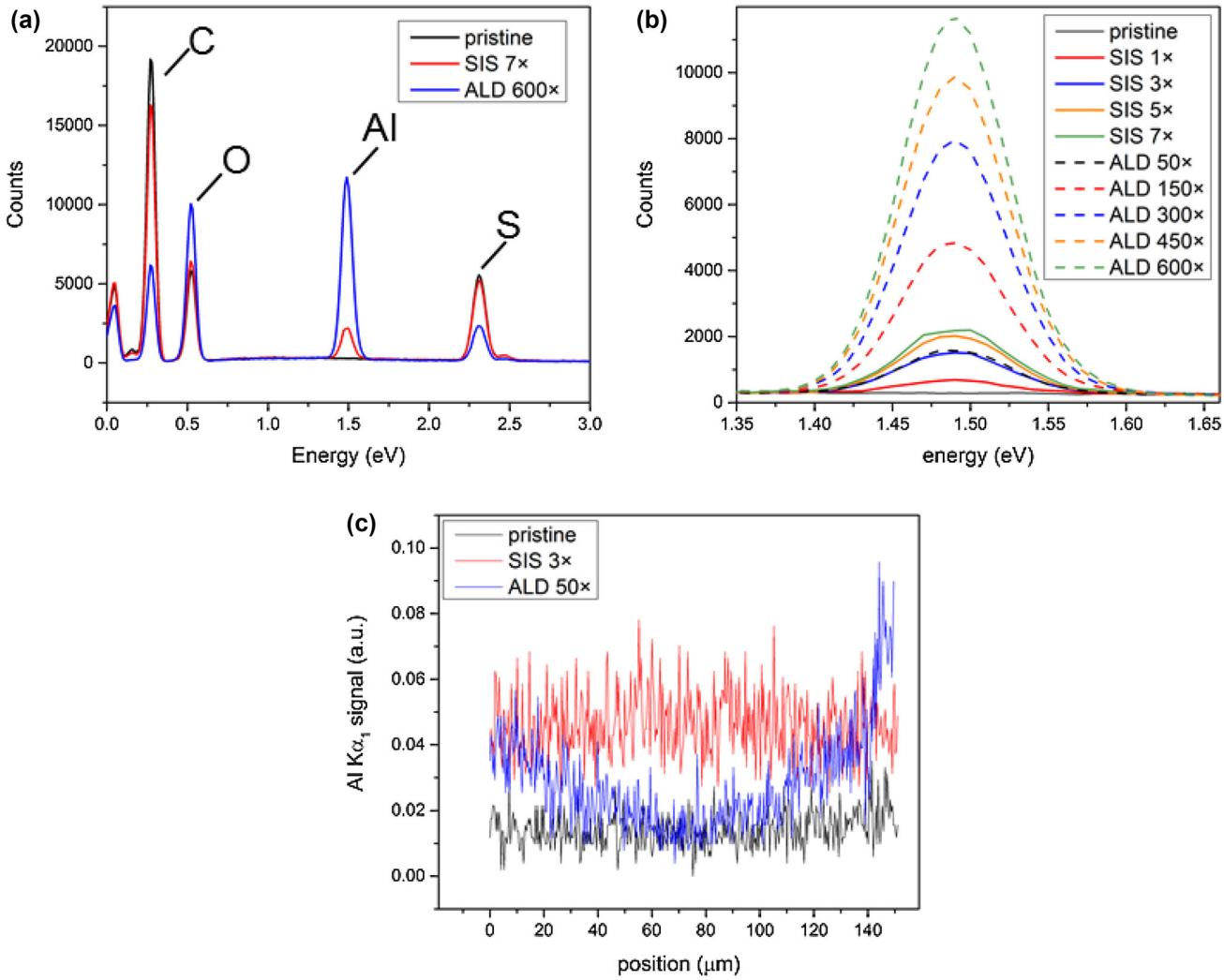


Fig. 8. EDS spectra of the top surfaces of PES membranes: (a) pristine, seven cycles SIS, and 600 cycles ALD demonstrate the appearance of an aluminum peak at 1.486 eV; (b) the Al EDS peak increases continuously with ALD cycles but saturates after five SIS cycles. Three SIS cycles and 50 ALD cycles yield similar intensities. (c) Cross-sectional EDS line scans reveal a uniform aluminum signal following three SIS cycles. In contrast, 50 ALD cycles show high Al EDS signals at the edges but no change from the uncoated membrane signal at the center, consistent with diffusion-limited coating.

compared to the bulk infiltration of polymer that is possible with SIS processing. This phenomenon explains the sensitivity of flux to the first five SIS cycles. The polymer continues to swell as active sites are consumed, which constricts the membrane pore volume significantly. After five cycles, the membrane is sufficiently swollen with $Al_2O_3$ that infiltration ceases, either because sites within the polymer are consumed or are inaccessible due to the oxide formed in previous cycles. $Al_2O_3$ deposited in SIS cycles after this occurs may be limited to the surface or interfaces of the already infiltrated oxide, leading to a significantly reduced material gain per cycle. The ALD-processed membranes show a roughly linear flux decline with number of cycles, consistent with minimal infiltration into the polymer. SEM images of the modified membrane surfaces are included in Supplementary Fig. S-10. These images show that, at least from the surface, pore constriction is difficult to quantify or directly observe due to pore polydispersity. We therefore infer from the flux decline that pores are gradually shrunk by $Al_2O_3$ surface growth layer-by-layer outward from the pore wall.

Elemental analysis by EDS was conducted to probe the incorporation of $Al_2O_3$ into the membrane. Figure 8a shows EDS spectra of the top surface of pristine membrane, 7 SIS cycles, and 600 ALD cycles. Notably, the Al peak at 1.486 eV is absent in the pristine polymer and emerges in the processed polymer. Figure 8b shows a close-up of the Al peak. The peaks of 3 SIS cycles and 50 ALD cycles are similar, much like how they exhibit similar levels of flux decline. EDS maps of the cross-sectional distribution of $Al_2O_3$ in pristine, 3 SIS, and 50 ALD cycles are shown in Fig. 8c. The distribution of the SIS samples is uniform throughout the membrane thickness, whereas the 50 ALD cycle membrane shows a slight decrease in signal at the center of the membrane. This asymmetry is a function of the short exposure doses conducted in the ALD process. The highly tortuous and high-aspect-ratio pore paths in UF membranes can lead to diffusion-limited deposition.[41,53,55] This asymmetric deposition may be a desirable feature in certain applications, such as in the formation of Janus materials.[42] Such asymmetry may be avoided by lengthening the timescales of vapor exposure within the ALD regime.

## CONCLUSION

This report explores the sequential infiltration synthesis of trimethylaluminum into a previously undescribed polymer system, polyethersulfone, which is widely used in membrane filtration. In situ FTIR of TMA in-diffusion and out-diffusion of this system identified the nature and kinetics of an attractive interaction between the TMA and the PES moieties, which leads to slow out-diffusion as observed in other successful SIS-polymer systems. Investigations of the spectral shifts caused by TMA confirm that the sulfonyl moiety in PES behaves, similar to the carbonyl in PMMA, as a Lewis basic site that can complex with the Lewis acidic TMA. These insights into the chemical interactions between vapor precursors and PES are supported by in situ ellipsometry measurements that reveal the kinetics of infiltration, saturation, and out-diffusion on the second time-scale. The thickness change of PES films, along with the aluminum content of these films as measured by depth-profiled XPS, confirm the strong role that purge time plays in the resulting polymer-metal oxide hybrid nanocomposite, especially in the short-purge time limit. Insights gained from this characterization are applied to PES ultrafiltration membranes to demonstrate SIS in a highly tortuous networked system. The loading of oxide per cycle is inferred to be much higher over the first five cycles of SIS than in subsequent cycles, as the pure water flux through the modified membrane declines and then stabilizes due to pore constriction. A similar intensity in EDS signal between 3 SIS cycles and 50 ALD cycles highlights the efficient bulk infiltration of SIS in contrast to the surface-limited nature of ALD. PES membranes infiltrated with metal oxides by SIS can enable the stable grafting of other molecules throughout the pore volume of the membrane, introducing new functionalities for advanced filtration applications.

## ACKNOWLEDGEMENTS

Use of the Center for Nanoscale Materials, an Office of Science user facility, was supported by the U.S. Department of Energy, Office of Science, Office of Basic Energy Sciences, under Contract No. DE-AC02-06CH11357. This material was based upon work supported by Laboratory Directed Research and Development (LDRD) funding from Argonne National Laboratory, provided by the Director, Office of Science, of the U.S. Department of Energy under Contract No. DE-AC02-06CH11357. This work made use of the Pritzker Nanofabrication Facility of the Institute for Molecular Engineering at the University of Chicago, which receives support from Soft and Hybrid Nanotechnology Experimental (SHyNE) Resource (NSF ECCS-1542205), a node of the National Science Foundation's National Nanotechnology Coordinated Infrastructure. Parts of this work were carried out at the Soft Matter Characterization Facility of the University of Chicago. The authors also acknowledge the MRSEC Shared User Facilities at the University of Chicago (NSF DMR-1420709) and the Geophysical Sciences Division at the University of Chicago.

## ELECTRONIC SUPPLEMENTARY MATERIAL

The online version of this article (https://doi.org/10.1007/s11837-018-3142-3) contains supplemen-

tary material, which is available to authorized users.

## REFERENCES


1. Q. Peng, Y.C. Tseng, S.B. Darling, and J.W. Elam, *Adv. Mater.* 22, 5129 (2010).
2. Q. Peng, Y.C. Tseng, S.B. Darling, and J.W. Elam, *ACS Nano* 5, 4600 (2011).
3. J. Frascaroli, E. Cianci, S. Spiga, G. Seguini, and M. Perego, *ACS Appl. Mater. Interfaces* 8, 33933 (2016).
4. M. Biswas, J.A. Libera, S.B. Darling, and J.W. Elam, *Chem. Mater.* 26, 6135 (2014).
5. M. Biswas, J.A. Libera, S.B. Darling, and J.W. Elam, *J. Phys. Chem. C* 119, 14585 (2015).
6. B. Gong and G.N. Parsons, *J. Mater. Chem.* 22, 15672 (2012).
7. E.C. Dandley, C.D. Needham, P.S. Williams, A.H. Brozena, C.J. Oldham, and G.N. Parsons, *J. Mater. Chem. C.* 2, 9416 (2014).
8. C.Z. Leng and M.D. Losego, *Mater. Horiz.* 4, 747 (2017).
9. R.P. Padbury and J.S. Jur, *J. Vac. Sci. Technol. A* 33, 01A112 (2015).
10. G.N. Parsons, S.E. Atanasov, E.C. Dandley, C.K. Devine, B. Gong, J.S. Jur, K. Lee, C.J. Oldham, Q. Peng, J.C. Spagnola, and P.S. Williams, *Coord. Chem. Rev.* 257, 3323 (2013).
11. C.-Y. Nam, A. Stein, and K. Kisslinger, *J. Vac. Sci. Technol. B* 33, 06F201 (2015).
12. C.-Y. Nam, A. Stein, K. Kisslinger, and C.B. Black, *Appl. Phys. Lett.* 107, 203106 (2015).
13. C.-Y. Nam and A. Stein, *Adv. Opt. Mater.* 5, 1 (2017).
14. J. Yin, Q. Xu, Z. Wang, X. Yao, and Y. Wang, *J. Mater. Chem. C* 1, 1029 (2013).
15. R. Ruiz, L. Wan, J. Lille, K.C. Patel, E. Dobisz, D.E. Johnston, K. Kisslinger, and C.B. Black, *J. Vac. Sci. Technol. B* 30, 06F202 (2012).
16. D. Berman, S. Guha, B. Lee, J.W. Elam, S.B. Darling, and E.V. Shevchenko, *ACS Nano* 11, 2521 (2017).
17. C. Zhou, T. Segal-Peretz, M.E. Oruc, H.S. Suh, G. Wu, and P.F. Nealey, *Adv. Funct. Mater.* 27, 1701756 (2017).
18. Y.C. Tseng, Q. Peng, L.E. Ocola, D.A. Czaplewski, J.W. Elam, and S.B. Darling, *J. Vac. Sci. Technol. B* 29, 06FG01 (2011).
19. Y.C. Tseng, A.U. Mane, J.W. Elam, and S.B. Darling, *Adv. Mater.* 24, 2608 (2012).
20. K.J. Dusoe, X. Ye, K. Kisslinger, A. Stein, S.-W. Lee, and C.-Y. Nam, *Nano Lett.* 17, 7416 (2017).
21. H.I. Akyildiz, M. Lo, E. Dillon, A.T. Roberts, H.O. Everitt, and J.S. Jur, *J. Mater. Res.* 29, 2817 (2014).
22. E. Barry, J.A. Libera, A.U. Mane, J.R. Avila, D. DeVitis, K. Van Dyke, J.W. Elam, and S.B. Darling, *Environ. Sci. Water Res. Technol.* 4, 40 (2018).
23. E. Barry, A.U. Mane, J.A. Libera, J.W. Elam, and S.B. Darling, *J. Mater. Chem. A* 5, 2929 (2017).
24. T. Segal-Peretz, J. Winterstein, M. Doxastakis, A. Ramirez-Hernandez, M. Biswas, J. Ren, H.S. Suh, S.B. Darling, J.A. Liddle, J.W. Elam, J.J. de Pablo, N.J. Zaluzec, and P.F. Nealey, *ACS Nano* 9, 5333 (2015).
25. G. Liu, M.P. Stoykovich, S. Ji, K.O. Stuen, G.S.W. Craig, and P.F. Nealey, *Macromolecules* 42, 3063 (2009).
26. R.B. Rigby, *Engineering Thermoplastics: Properties and Applications* (New York: Marcel Dekker, 1985).
27. A.L. Ahmad, A.A. Abdulkarim, B.S. Ooi, and S. Ismail, *Chem. Eng. J.* 223, 246 (2013).
28. C. Zhao, J. Xue, F. Ran, and S. Sun, *Prog. Mater. Sci.* 58, 76 (2013).
29. J.F. Li, Z.L. Xu, H. Yang, L.Y. Yu, and M. Liu, *Appl. Surf. Sci.* 255, 4725 (2009).
30. N. Maximous, G. Nakhla, K. Wong, and W. Wan, *Sep. Purif. Technol.* 73, 294 (2010).
31. S. Simone, F. Galiano, M. Faccini, M. Boerrigter, C. Chaumette, E. Drioli, and A. Figoli, *Fibers* 5, 14 (2017).
32. A. Razmjou, J. Mansouri, V. Chen, M. Lim, and R. Amal, *J. Membr. Sci.* 380, 98 (2010).
33. H. Chen, L. Kong, and Y. Wang, *J. Membr. Sci.* 487, 109 (2015).
34. Q. Xu, Y. Yang, J. Yang, X. Wang, Z. Wang, and Y. Wang, *J. Membr. Sci.* 443, 62 (2013).
35. F. Li, L. Li, X. Liao, and Y. Wang, *J. Membr. Sci.* 385–386, 1 (2011).
36. Q. Wang, X. Wang, Z. Wang, J. Huang, and Y. Wang, *J. Membr. Sci.* 442, 57 (2013).
37. S.J. Yu, J.W. Lim, and J.-H. Lee, *Electrochem. Sloid State Lett.* 7, C13 (2004).
38. P.E. Petrochenko, G. Scarel, G.K. Hyde, G.N. Parsons, S.A. Skoog, Q. Zhang, P.L. Goering, and R.J. Narayan, *JOM* 65, 550 (2013).
39. T. Cheng, H. Chen, S. Xiong, X. Chen, and Y. Wang, *AIChE J.* 60, 3614 (2014).
40. R.Z. Waldamn, H.-C. Yang, D.J. Mandia, P.F. Nealey, J.W. Elam, and S.B. Darling, *Adv. Mater. Interfaces* 5, 1800658 (2018).
41. J.W. Elam, J.A. Libera, M.J. Pellin, and P.C. Stair, *Appl. Phys. Lett.* 91, 177 (2007).
42. W.-H. Lau, M. Guiver, and T. Matsuura, *J. Membr. Sci.* 59, 219 (1991).
43. D.J. Comstock and J.W. Elam, *J. Phys. Chem. C* 117, 1677 (2013).
44. X. Ye, K. Kisslinger, M. Liu, R.B. Grubbs, J.A. Boscoboinik, and C.-Y. Nam, *Chem. Mater.* 29, 4535 (2017).
45. M.J. Frisch, G.W. Trucks, H.B. Schlefel, G.E. Scuseria, M.A. Robb, J.R. Cheeseman, G. Scalmani, B. Barone, B. Mennucci, G.A. Petersson, H. Nakatsuji, M. Caricato, X. Li, H.P. Hratchian, A.F. Izmaylov, J. BLoino, G. Zheng, J.L. Sonnenberg, M. Hada, M. Ehara, K. Toyota, R. Fukuda, J. Hasegawa, M. Ishida, T. Nakajima, Y. Honda, O. Kitao, H. Nakai, T. Vreven, J.A. Montgomery Jr., J.E. Peralta, F. Oligaro, M. Bearpark, J.J. Heyd, E. Brothers, K.N. Kudin, V.N. Staroverov, R. Kobayashi, J. Normand, K. Raghavachari, A. Rendell, J.C. Burant, S.S. Ivengar, J. Tomasi, M. Cossi, N. Rega, N.J. Millam, M. Klene, J.E. Knox, J.B. Cross, V. Bakeen, C. Adamo, J. Jaramillo, R. Gomperts, R.E. Stratmann, O. Yazyev, A.J. Austin, R. Cammi, C. Pomelli, J.W. Ochterski, R.L. Martin, K. Morokuma, V.G. Zakrzewski, G.A. Voth, P. Salvador, J.J. Dannenberg, S. Dapprich, A.D. Daniels, Ö. Farkas, J.B. Foresman, J.V. Ortiz, J. Cioslowski, and D.J. Fox, Gaussian 09, Revision A.02; Gaussian, Inc.: Wallingford, CT (2009).
46. M. Fontyn, K. van't Riet, and B.H. Bijsterbosch, *Colloids Surf.* 54, 331 (1991).
47. M.L. Mendez, A.I. Romero, V.B. Rajal, E.F. Castro, J.I. Calvo, L. Palacio, and A. Hernandez, *Polym. Eng. Sci.* 54, 1211 (2014).
48. J.H. Choi, J. Jegal, and W.N. Kim, *J. Membr. Sci.* 285, 406 (2006).
49. D.G. Goldstein, J.A. McCormick, and S.M. George, *J. Phys. Chem. C* 112, 19530 (2008).
50. G.A. Atiya, A.S. Grady, D.K. Russell, and T.A. Claxton, *Spectrochim. Acta Part A Mol. Spectrosc.* 47, 467 (1991).
51. B.G. Frederick, G. Apai, and T.N. Rhodin, *Phys. Rev. B* 44, 1880 (1991).
52. K. Sollia, M. Ystenes, and P. Sobotab, *Proc. SPIE* 1575, 608 (1991).
53. Q. Xu, J. Yang, J. Dai, Y. Yang, X. Chen, and Y. Wang, *J. Membr. Sci.* 448, 215 (2013).
54. A. Lee, J.A. Libera, R.Z. Waldman, A. Ahmed, J.R. Avila, J.W. Elam, and S.B. Darling, *Adv. Sustain. Syst.* 1, 1600041 (2017).
55. A. Yanguas-Gil and J.W. Elam, *Chem. Vap. Depos.* 18, 46 (2012).